A novel approach for wave-turbulence decomposition

Lin, Jianliang; Zhu, Chunyan; Sun, Jianwei; Xie, Weiming; van Prooijen, Bram; Guo, Leicheng; He, Qing; Yang, Qingshu; Wang, Zheng Bing

DOI
10.1016/j.coastaleng.2025.104807

Publication date
2025

Document Version
Final published version

Published in
Coastal Engineering

Citation (APA)
Lin, J., Zhu, C., Sun, J., Xie, W., van Prooijen, B., Guo, L., He, Q., Yang, Q., & Wang, Z. B. (2025). A novel approach for wave-turbulence decomposition. *Coastal Engineering*, *201*, Article 104807. https://doi.org/10.1016/j.coastaleng.2025.104807

Coastal Engineering 201 (2025) 104807

Contents lists available at ScienceDirect

Coastal Engineering

journal homepage: www.elsevier.com/locate/coastaleng

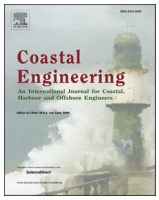

A novel approach for wave-turbulence decomposition

Jianliang Lin [a,b,c,*], Chunyan Zhu [b], Jianwei Sun [c], Weiming Xie [b], Bram van Prooijen [c], Leicheng Guo [b], Qing He [b,**], Qingshu Yang [a], Zheng Bing Wang [b,c,d]

[a] School of Marine Engineering and Technology, Sun Yat-sen University, 619082, Zhuhai, China
[b] State Key Laboratory of Estuarine and Coastal Research, East China Normal University, 200241, Shanghai, China
[c] Delft University of Technology, 2628 CN, Delft, Netherlands
[d] Deltares, 2629 HV, Delft, Netherlands

ARTICLE INFO

Keywords:
Wave
Turbulence
Turbulent kinetic energy
Energy spectrum

ABSTRACT

Decomposing turbulence from waves remains challenging due to frequency overlap and wave-turbulence interactions. Existing decomposition methods, e.g., moving average, energy spectrum analysis, and synchrosqueezed wavelet transform (SWT), produce inconsistent turbulence estimates. Here, we introduce a rotating-coordinate-based method (RoCoM), founded on two assumptions: (1) the energy spectrum in the cross-wave direction remains unaffected by wave orbital velocities, and (2) wave-wise and vertical turbulence spectra are linearly proportional to the cross-wave spectrum, with proportional constants derived from frequencies higher than the wave-dominated frequency range. Both assumptions were validated with observational data collected from the Changjiang Estuary. Comparative analyses using both in-situ observations and controlled laboratory experiments show RoCoM avoids the energy trough problem inherent in the moving average and SWT methods, yielding the most accurate power spectra and turbulent kinetic energy (TKE) estimates. In-situ data reveal that the relative errors of RoCoM are approximately 16 % for total TKE and about 6 % for TKE within the wave-dominated frequency range. Laboratory experiments further confirm its superior accuracy, demonstrating relative errors of approximately 14 % for total TKE and about 7 % for wave-band TKE. RoCoM holds significant implications for marine material transport and coastal energy development by providing robust and precise turbulence and wave energy estimates. Nonetheless, its application is currently best suited for scenarios with predominant wave propagation from a single direction, while SWT remains advantageous in environments characterized by broader directional wave spreading.

1. Introduction

Turbulence is common in aquatic environments and is crucial in transporting pollutants, nutrients, and sediment. Accurate estimation of turbulence parameters (e.g., turbulent Reynolds stress and kinetic energy) is critical to quantify turbulence effects on hydrodynamics (e.g., density stratification and mixing), sediment resuspension, and carbon emission in benthic boundary layers (Amoudry and Souza, 2011; Li et al., 2022; Song et al., 2022). Additionally, precise assessments of turbulence and wave energy are essential for designing and maintaining the long-term functionality of tidal turbines (Copping et al., 2014; Harrold and Ouro, 2019; McCaffrey et al., 2015).

However, quantifying turbulence characteristics in wavy environments remains challenging due to the overlap of turbulence and wave orbital motions within a particular frequency subrange. In coastal zones with long surface gravity waves or shallow depths, orbital motions can reach deeper water layers and influence turbulent velocity fluctuations. Waves generally bias turbulence parameter estimation in two primary ways. First, as turbulent eddies are advected by both mean flow and wave orbital velocities, wave orbital motions significantly affect Eulerian turbulence measurements, especially under severe wave conditions (Lumley and Terray, 1983; Rosman and Gerbi, 2017). Second, the nonlinearity of waves or uncertainties in instrument tilts can cause significant covariance between horizontal and vertical velocities, leading to biased estimates of turbulent Reynolds stress (Trowbridge, 1998). Effectively eliminating these wave-induced biases remains challenging (Bricker and Monismith, 2007; Kirincich et al., 2010; Rosman et al., 2008). To date, wave-turbulence decomposition methods can be

* Corresponding author. School of Marine Engineering and Technology, Sun Yat-sen University, 619082, Zhuhai, China.
** Corresponding author.
E-mail addresses: linjliang7@mail.sysu.edu.cn (J. Lin), qinghe@sklec.ecnu.edu.cn (Q. He).

https://doi.org/10.1016/j.coastaleng.2025.104807
Received 3 March 2025; Received in revised form 17 May 2025; Accepted 10 June 2025
Available online 11 June 2025

categorized into six primary approaches: coherence, cospectra, linear wave theory, empirical mode decomposition, moving average, and energy spectrum analysis. These methods rely on different physical assumptions and mathematical algorithms.

The coherence method assumes wave parameters (e.g., wave-induced surface elevation and orbital velocity) are coherent, whereas turbulent velocity fluctuations are uncorrelated with waves. This category includes elevation-velocity coherence (Benilov et al., 1974), two-point velocity coherence (Shaw and Trowbridge, 2001; Trowbridge, 1998), and the phase method (Bricker and Monismith, 2007). The elevation-velocity coherence method attributes the velocity component correlated with surface elevation variations to waves, with the remaining component classified as turbulent fluctuations. Similarly, the two-point velocity coherence method considers coherent velocities at two points as wave motions and the residual component as turbulence. These two techniques require multiple measurement probes. To improve practicality, Bricker and Monismith (2007) proposed the phase method, which estimates wave-induced shear stress using the phase lag between horizontal and vertical velocities at wave-dominated frequencies based on single-probe velocity measurements. This method has been widely adopted in subsequent studies (Brand et al., 2010; MacVean and Lacy, 2014).

The cospectra method is based on turbulence theories. According to the Kolmogorov theory, the power spectral density of turbulent velocity follows a power law of $-5/3$ to wavenumber (k) or frequency (f) in the inertial subrange (Frisch, 1995). Likewise, the cospectrum between horizontal and vertical velocities is nearly constant at low wavenumbers and decreases following a $k^{-7/3}$ scaling in the inertial subrange (Kaimal et al., 1972). Based on this cospectrum model, Gerbi et al. (2008) developed the cospectra method for estimating Reynolds stress using acoustic Doppler velocimeter (ADV) measurements. By fitting low-wavenumber cospectra to an empirical model, this approach estimates both Reynolds stress and roll-off wavenumber. The method has also been extended to acoustic Doppler current profiler measurements (Kirincich, 2013; Kirincich et al., 2010; Kirincich and Rosman, 2011). However, the cospectra method is applicable only under weak wave conditions, where wave orbital velocity remains lower than the mean flow velocity (Rosman and Gerbi, 2017). In stronger wave conditions, wave advection significantly modifies the velocity cospectra, invalidating the empirical cospectrum model.

Recently, Perez et al. (2020b) developed a linear wave theory method, which estimates wave orbital velocities from surface elevation data. Wave-turbulence decomposition is then achieved by subtracting these wave orbital velocities from the total velocity signal. However, this method is less effective in high-frequency wave conditions or when wave energy is distributed across a broad frequency range (Perez et al., 2020b).

The empirical mode decomposition method separates waves and turbulence by decomposing the original signals into a sequence of intrinsic mode functions (IMFs). This category includes stopband filtering (Perez et al., 2020a), empirical mode decomposition (EMD; Huang et al., 1998; Qiao et al., 2016), ensemble empirical mode decomposition (EEMD; Wu and Huang, 2009; 2004), and synchrosqueezed wavelet transform (SWT; Bian et al., 2018). The stopband method isolates wave components via Fourier transform filtering. Although widely used for estimating turbulent intensity, recent studies highlight the limitations of high-pass or band-pass filters in eliminating wave interference (Perez et al., 2020a; Zhu et al., 2016). When a high-pass filter is employed, the stopband method resembles the moving average (MA) method.

The EMD method, designed for analyzing nonlinear and non-stationary time-series data, decomposes signals into IMFs through a sifting process, where each IMF represents a narrowband frequency-amplitude modulation (Huang et al., 1998, 2016). Qiao et al. (2016) applied this method to estimate Reynolds stress in wavy environments. However, EMD suffers from mode-mixing, where an IMF may contain disparate frequency signals or a signal of a specific scale may be distributed across multiple IMFs (Huang et al., 2003). The EEMD mitigates this issue by introducing white noise ensembles into the sifting process (Wang et al., 2014; Wu and Huang, 2004, 2009).

The SWT method, similar to EMD, decomposes signals in a time-frequency plane, but is based on the wavelet transform and reallocation method (Daubechies et al., 2011; Thakur et al., 2013). Turbulent fluctuations are estimated by subtracting components within the wave-dominated frequency range. However, this approach removes turbulence components within the frequency range, producing an artificial "energy trough" in turbulent spectra, leading to underestimated turbulent fluctuations (Bian et al., 2018; Perez et al., 2020a).

To address the "energy trough" problem, we propose a rotating-coordinate-based method (RoCoM) for wave-turbulence decomposition. Like the energy spectrum analysis (ESA) method, RoCoM separates waves and turbulence in a spectral plane. This approach assumes that wave orbital velocities do not influence the cross-wave direction energy spectrum ($S_{v\beta1}$), which has the lowest power spectral density at wave frequencies. Additionally, we assume that wave-wise ($S_{u\beta1}$) and vertical ($S_{w\beta1}$) turbulence spectra are linearly proportional to $S_{v\beta1}$ at wave frequencies, with proportional constants estimated at higher frequencies. Based on these assumptions, $S_{u\beta1}$ and $S_{w\beta1}$ at wave frequencies are determined, mitigating the "energy trough" problem. Subtracting the turbulent spectrum from the original yields the wave-related velocity spectrum, achieving wave-turbulence decomposition.

This study compares RoCoM with MA, ESA, and SWT methods regarding power spectra and turbulent kinetic energy (TKE) estimation. Coherence, cospectra, linear wave theory, stopband, and EEMD methods are omitted due to their greater uncertainty than SWT (Bian et al., 2018; Perez et al., 2020a, 2020b). Observational data from the Changjiang (Yangtze) Estuary and laboratory experiments (Section 2.1) are used to validate RoCoM assumptions. Section 2.2 introduces RoCoM, MA, ESA, and SWT methods. Section 3 presents performance comparisons, advantages, and limitations. Finally, conclusions are provided in Section 4.

2. Materials and methods

2.1. Data for method evaluation

2.1.1. In-situ observations

This study employs observational data collected in the Changjiang Estuary from January 15 to 29, 2016. The measurement site was in the North Passage (Fig. 1), with an average water depth of approximately 11 m (Fig. 2a). A bottom-mounted tripod system was deployed, equipped with a downward-looking ADV (Nortek Vector) positioned at 0.35 m above the bed (mab) and three optical backscattering sensors (OBSs; D&A Instruments, model 3A) located at 0.35, 0.55, and 1.06 mab (Table 1). The ADV was configured to record burst measurements at a sampling frequency of 16 Hz, each lasting 90 s, and collected every 5 min. Velocities and pressure measurements recorded by the ADV were despiked and denoised using the Phase-Space method (Goring and Nikora, 2002). Wave heights and periods were computed from corrected pressure data employing standard spectral methods (Tucker and Pitt, 2001; Wiberg and Sherwood, 2008). Additionally, near-bed wave orbital velocities (root-mean-square, rms) were estimated from the velocity spectra following Wiberg and Sherwood (2008).

The OBS sensors were positioned at 0.35, 0.55, and 1.06 mab, measuring turbidity, salinity, and temperature every 5 min. These data were used to compute the buoyancy frequency (N^2) to quantify water column stratification as follows:

$$N^2 = \frac{g}{\rho}\frac{\partial \rho}{\partial z} \tag{1}$$

where g is gravitational acceleration (9.8 m/s^2), ρ is the density of sediment-laden water, and z indicates height above the seabed. The

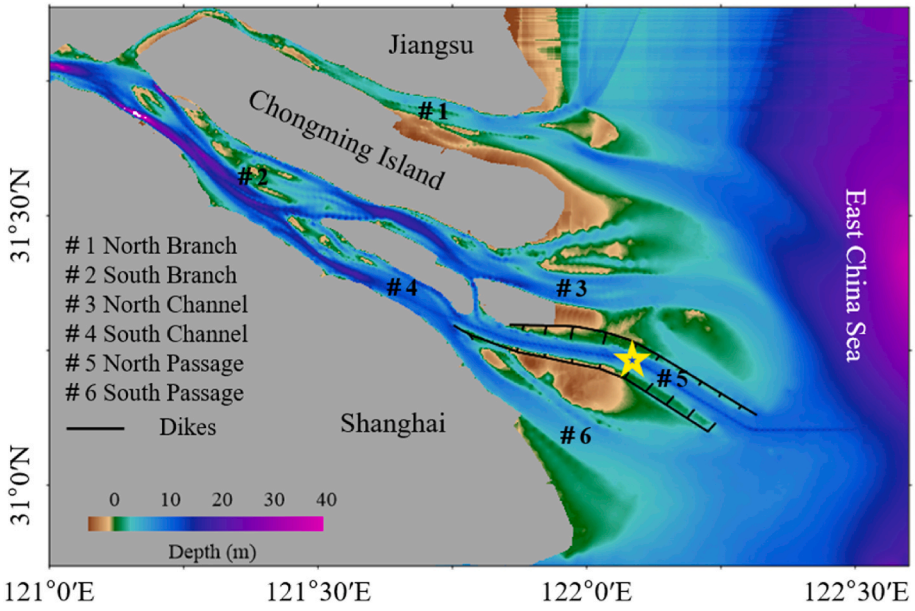

Fig. 1. Bathymetry of the Changjiang Estuary and adjacent regions. The yellow star indicates the measuring site in the North Passage. (For interpretation of the references to colour in this figure legend, the reader is referred to the Web version of this article.)

sediment-laden water density (ρ) was estimated using:

$$\rho = \rho_w(T,S) + \left(1 - \frac{\rho_w(T,S)}{\rho_s}\right) C \tag{2}$$

where ρ_w is seawater density calculated from temperature (T) and salinity (S) following the formula provided by Millero and Poisson (1981), ρ_s is the density of suspended sediments (2570 kg/m^3 typical for the Changjiang Estuary; Guo et al., 2017), and C is the suspended sediment concentration derived from OBS turbidity measurements calibrated with local sediment samples (Lin et al., 2020).

Throughout the observational campaign, spectral analyses of water-level data revealed prominent wave energy between 0.05 Hz and 0.5 Hz (Fig. 2e). The dominant wave periods, corresponding to peak spectral energy, ranged from 4 to 7 s (Fig. 2d). A significant windstorm occurred from January 23 to 25, characterized by strong northeast (0°–90°) winds with peak wind speeds reaching 18 m/s (Fig. 2c). During this storm, the maximum wave height reached approximately 1.4 m.

2.1.2. In-lab measurements

Controlled laboratory experiments were conducted to provide a robust reference dataset for evaluating wave-turbulence decomposition methods. The experiments included conditions with and without waves, allowing the no-wave scenario to serve as a baseline or control condition. These experiments were performed in a wave-current flume at the School of Ocean Engineering and Technology, Sun Yat-sen University.

The flume dimensions were 16 m in length, 0.4 m in width, and 0.5 m in height (Fig. 3). A variable-speed pump was employed to generate steady unidirectional flows, with a consistent flow velocity of 0.6 m/s maintained across all experimental conditions. Under wave conditions, monochromatic waves traveling in the same direction as a piston-type wave paddle generated the current. These waves had a fixed wave height of 0.1 m and a period of 2 s.

High-resolution velocity measurements were collected using a Nortek Vectrino Plus ADV, positioned precisely at the midpoint of the flume (8.0 m from both ends). The ADV probe was deployed downward-looking at 0.17 m above the channel bottom (Fig. 3), and velocities were measured at 0.12 m above the bottom (0.05 m from the ADV probe). Each experiment recorded velocities continuously at 32 Hz for 300 s (Table 1), ensuring comprehensive coverage across the frequency range required for accurate wave-turbulence analysis.

These laboratory conditions, enhanced sampling frequency (32 Hz) and duration (300 s), were specifically chosen to overcome the limitations of in-situ observations, providing a broader and more reliable frequency spectrum, thus significantly improving the evaluation accuracy of wave-turbulence decomposition methods.

2.2. Wave-turbulence decomposition methods

2.2.1. Rotating-coordinate-based method

The RoCoM developed in this study aims to separate turbulence from wave-induced velocities based on two fundamental assumptions. First, it assumes that waves do not significantly influence the cross-wave turbulent spectral density ($S_{v\beta 1}$). This assumption is primarily valid under conditions with narrow directional wave spreading, which are commonly observed near coastal regions, where waves typically approach nearly perpendicular to the shoreline (Herbers et al., 1999; Le Merle et al., 2021; Sundar et al., 1998). In these scenarios, the wave-induced cross-wave velocities are negligible compared to the corresponding turbulence-induced velocities, even though wave-wise and vertical wave orbital velocities are typically an order of magnitude larger. The cross-wave direction is identified by finding the direction in which the integrated power spectral density (PSD) at wave frequencies is minimal. While RoCoM effectively identifies the axial direction of wave motion, it does not determine the propagation direction. However, in environments with significant directional spreading, $S_{v\beta 1}$ becomes influenced by wave orbital velocities, compromising this assumption.

The second assumption posits that the wave-wise and vertical turbulent spectral densities are proportional to the cross-wave within the wave-frequency range for estimating TKE, thus implying a consistent three-dimensional (fractal) turbulence structure across frequencies. This assumption builds upon established turbulence spectra formulations for the wall region of unstratified boundary layers (Kaimal et al., 1972):

$$\frac{nS_{uu}}{u_*^2} = \frac{105f}{(1+33f)^{5/3}} \tag{3a}$$

$$\frac{nS_{vv}}{u_*^2} = \frac{17f}{(1+9.5f)^{5/3}} \tag{3b}$$

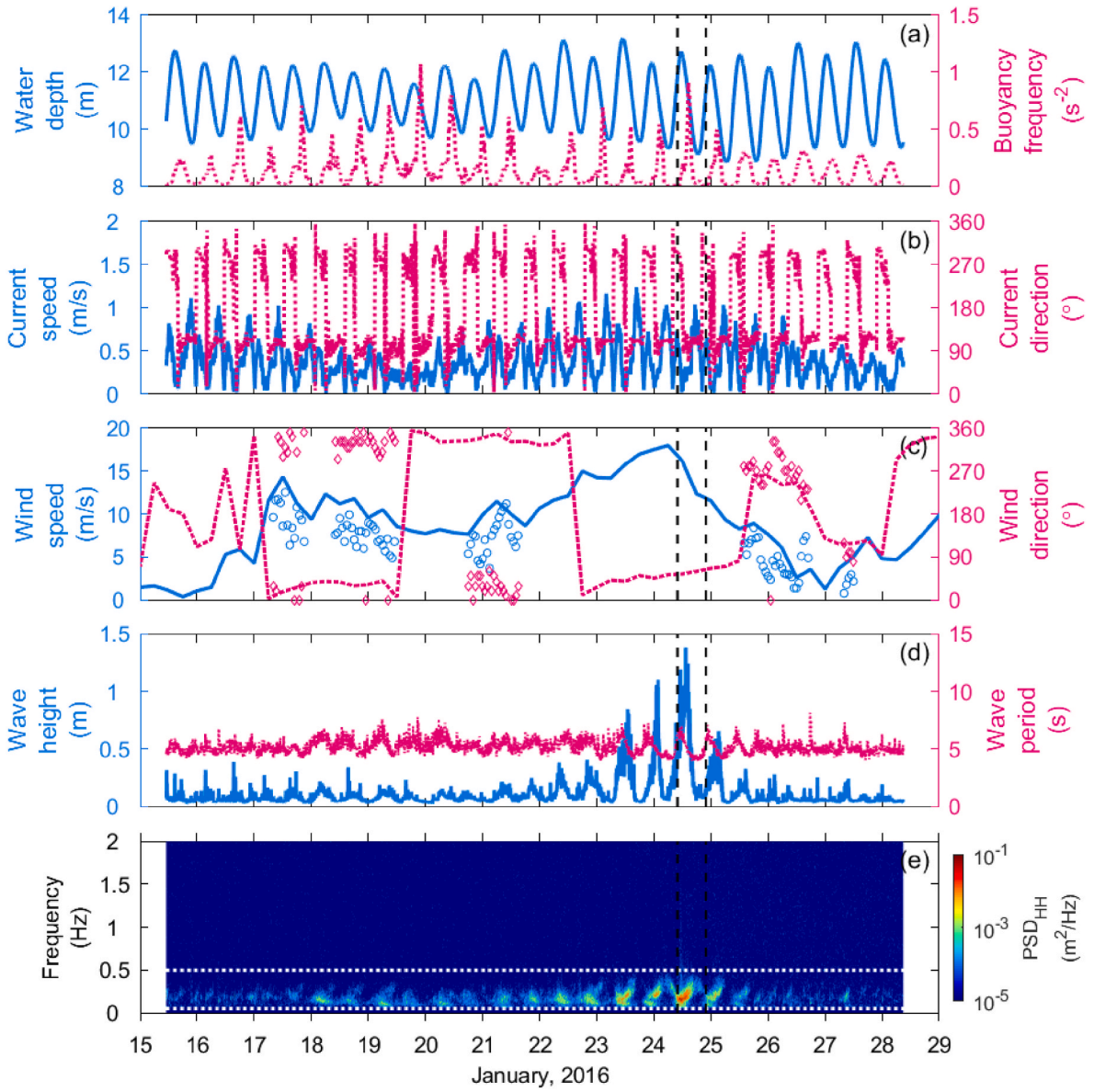

Fig. 2. Time series of (a) water depth (blue) and buoyancy frequency (red), (b) the magnitude (blue) and direction (red) of burst-averaged flow velocity, (c) wind speed (blue) and direction (red) and (d) significant wave height (blue) and period (red). In panel c, lines indicate the wind data obtained at 122.0°E and 31.5°N from the European Centre for Medium-Range Forecasts, validated by the measurements (dots) recorded by a hand-anemometer at 10 m above the sea surface. (e) The power spectra density (PSD) of surface elevation in a time-frequency plane. The dotted white lines indicate the boundaries of the wave-dominated frequency range used in our analysis, with the upper one for a frequency of 0.5 Hz and the lower one for a frequency of 0.05 Hz. The black lines indicate the bursts taken as examples to elaborate and evaluate the RoCoM method. (For interpretation of the references to colour in this figure legend, the reader is referred to the Web version of this article.)

Table 1
Details of data source for wave-turbulence decomposition method evaluation.

Observation type	Sensor	Distance above bed (m)	Sampling interval (min)	Sampling duration (sec)	Sampling frequency (Hz)	Parameters
In-situ measurements	Nortek Vector ADV	0.35	10	90	16	Velocity
	OBS-3A	0.35, 0.55, 1.06	5	60	1	Temperature, salinity, SSC
In-lab measurements	Nortek Vectrino Plus ADV	0.17	continuous	300	32	Velocity

$$\frac{nS_{ww}}{u_*^2} = \frac{2f}{1 + 5.3f^{5/3}} \tag{3c}$$

where n is the cyclic frequency, u^* is the shear velocity, f is frequency, and S_{uu}, S_{vv}, and S_{ww} represent stream-wise, cross-stream, and vertical turbulence spectra, respectively. These equations have a solid empirical

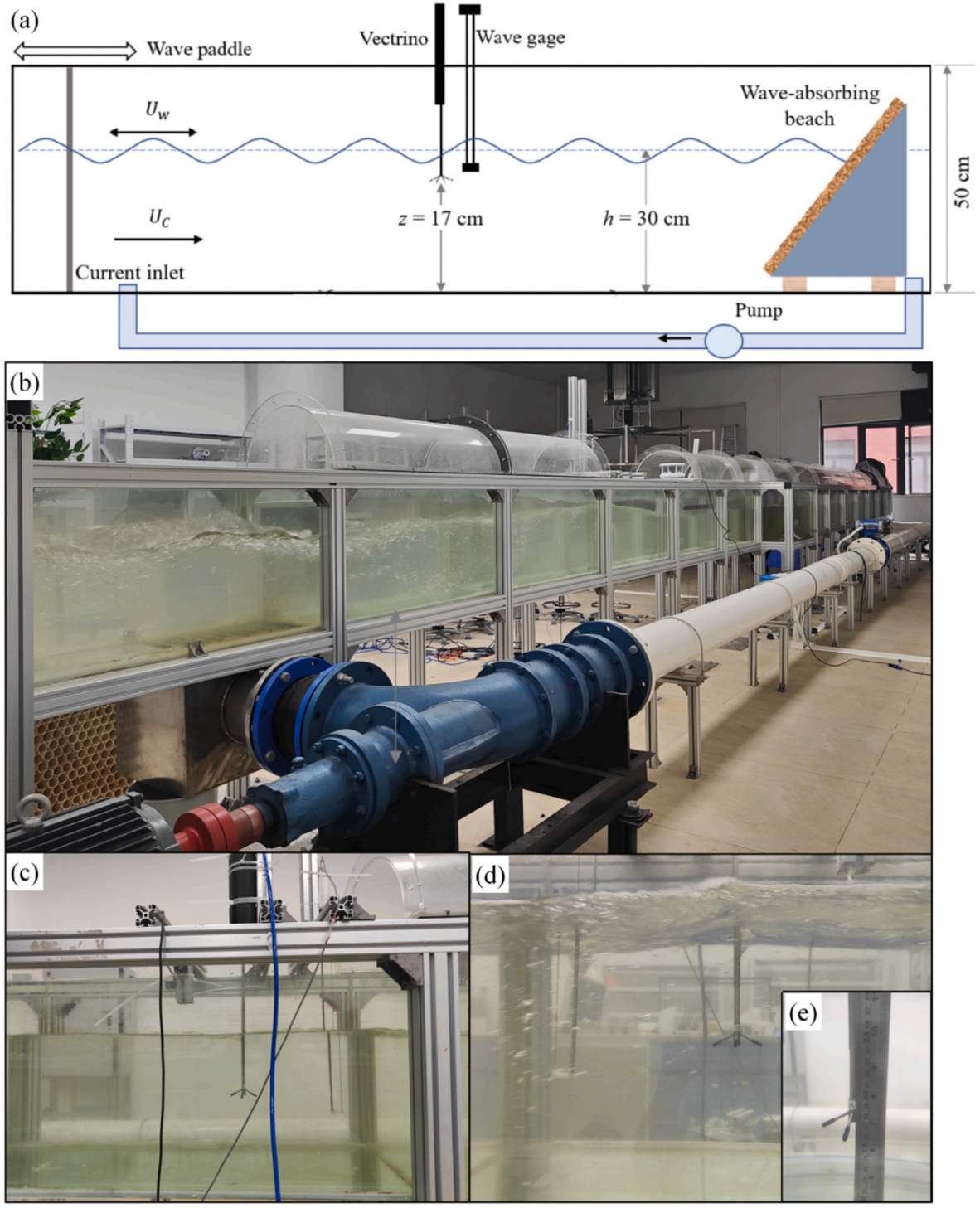

Fig. 3. Deployment of in-lab water channel experiments to collect data for the evaluation of wave-turbulence decomposition methods. (a) Schematic of the experiment, not to scale, with wave paddle and current inlet on the left, a wave-absorbing beach on the right, a wave gauge recording free-surface displacements, and a Nortek Vectrino Plus ADV measuring high-frequent velocities. (b) An overview of the water channel in the fluid mechanics lab at Sun Yat-sen University. (c) The deployment of ADV. (d) (e) Height of the ADV probe.

foundation and remain widely used in meteorology (e.g., Veers et al., 2019) and oceanography (e.g., Trowbridge and Lentz, 2018). As demonstrated empirically, these spectra maintain proportional relationships at high frequencies (Fig. 4a), with constants of approximately 0.78 (S_{uu}/S_{vv}) and 0.95 (S_{ww}/S_{vv}). These constants, multiplied by S_{vv}, yield S_{uu} and S_{ww} (Fig. 4b). Within the wave band (e.g., 0.05–0.5 Hz), S_{uu}/S_{vv} and S_{ww}/S_{vv} ratios vary significantly, yet integrating these relationships yields relatively accurate TKE estimates, with a relative error of −0.16 % (Table 2), due to the minor contribution of wave-band TKE to the total TKE. Given that wave-wise and cross-wave velocities can be resolved into stream-wise and cross-stream components, turbulence spectra in wave-wise ($S_{u\beta 1}$), cross-wave ($S_{v\beta 1}$), and vertical ($S_{w\beta 1}$) directions exhibit similar proportional relationships validated through observational data in the Changjiang Estuary (Fig. 5h–i).

The RoCoM separates turbulence from waves through the following six steps, illustrated by an ADV data example collected from the

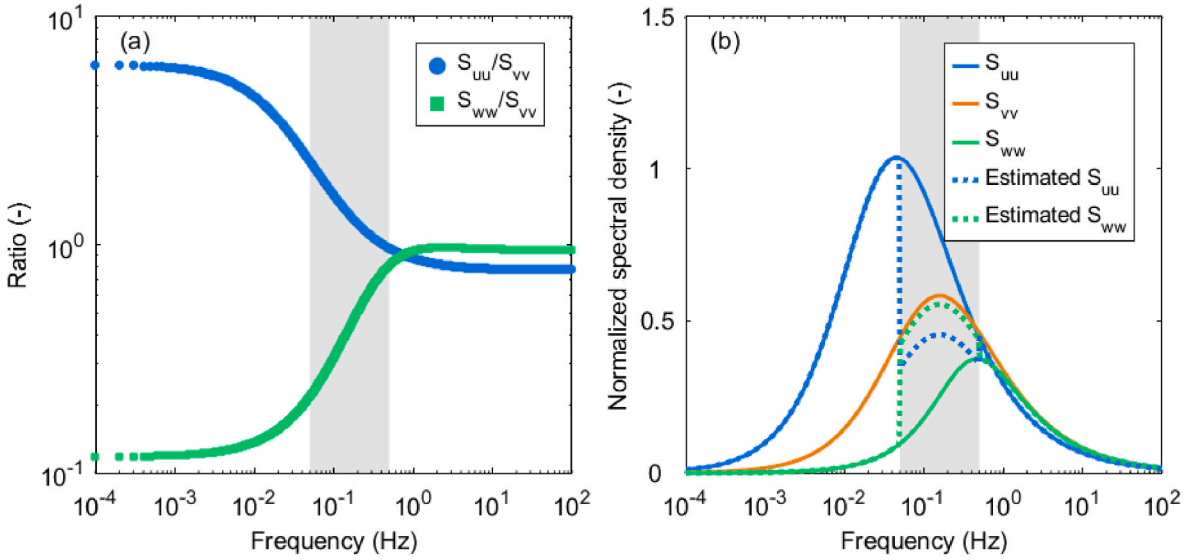

Fig. 4. (a) The ratios of wave-wise (S_{uu}) and vertical (S_{ww}) turbulent spectral density to cross-wave turbulent spectral density (S_{vv}) according to Equations (3a)-(3c) derived by Kaimal et al. (1972). (b) Turbulence spectra computed (solid lines) using Equations (3a)-(3c) and turbulence spectra estimated (dotted lines) by the RoCoM with wave-wise (S_{uu}) and vertical (S_{ww}) turbulence spectra at wave frequencies (grey areas) replaced by the product of cross-wave (S_{vv}) turbulence spectra and the proportional constants (i.e., S_{uu}/S_{vv} and S_{ww}/S_{vv}) estimated at high frequencies. The grey area shows the wave-dominated frequency range.

Table 2
The true values of S_{uu}/S_{vv} and S_{ww}/S_{vv} at wave frequencies and turbulent kinetic energy (TKE) from Equations (3a)-(3c) and the estimates given by the RoCoM. The parentheses show the range of values, and the values below are the averages. The estimates of S_{uu}/S_{vv} and S_{ww}/S_{vv} are the mean values at high frequencies outside the wave band. The subscripts in TKE indicate the *u*, *v*, and *w* components and their sum.

	S_{uu}/S_{vv}	S_{ww}/S_{vv}	$\frac{n}{u_*^2}\mathrm{TKE}_u$	$\frac{n}{u_*^2}\mathrm{TKE}_v$	$\frac{n}{u_*^2}\mathrm{TKE}_w$	$\frac{n}{u_*^2}\mathrm{TKE}_t$
True value	*(0.97, 2.33)*	*(0.22, 0.81)*	3.87	4.71	4.39	12.97
	1.23	0.58				
Estimate	*0.78*	*0.95*	3.76	4.71	4.48	12.95
Relatie error (%)	*−36.84*	*+63.26*	−2.84	0	+2.05	−0.16

Changjiang Estuary (burst No.2592, recorded at 10:55, January 24, 2016) .

(1) Identifying wave-dominated frequencies: The wave-dominated frequency range (f_{wl} = 0.05 Hz, f_{wu} = 0.5 Hz) is determined by using the ADV-recorded water level spectrum (Fig. 2e), where f_{wl} and f_{wu} denote the lower and upper frequency limits, respectively. A sampling frequency of at least 16 Hz is recommended to resolve potential overlaps between turbulence and wave frequencies.

(2) Despiking and coordinate transformation: Velocity data undergo despiking using the Phase-Space method (Goring and Nikora, 2002). Original velocities in the east, north, and vertical coordinates (U_E, U_N, U_U) are transformed into stream-wise, cross--stream, and vertical coordinates (U, V, W). Mean flow velocities are removed in this step, leaving only wave- and turbulence-induced fluctuations; these velocity fluctuations are collected in an ellipsoid (Fig. 5a). Since waves generate velocities significantly greater than turbulence, the long axis of the ellipsoid indicates the wave direction. The dashed vector (i.e., from (0, 0, 0) in U_E-U_N-U_U coordinates to (0, 0, 0) in U-V-W coordinates) indicates the mean flow.

(3) Rotating coordinate system: The coordinate system (U, V, W) is rotated first around the cross-stream axis (V) by an angle θ to achieve horizontal alignment (U_0, V_0, W_0), where U_0 and V_0 are in the horizontal plane and W_0 is vertically upward. The coordinate system is then horizontally rotated around the vertical axis (W_0) by an angle β (0°–360°) at increments of 1° to obtain (U_β, V_β, W_β). For each β, three-dimensional velocities obtained in the second step are then projected into the U_β-V_β-W_β coordinate system, and the spectra densities ($S_{u\beta}$, $S_{v\beta}$, $S_{w\beta}$) are derived through spectral analysis. Fig. 5b–c shows that $S_{u\beta}$ and $S_{v\beta}$ are a function of β, particularly at low frequencies. The cross-wave direction (β_1) is identified as the angle minimizing the integrated energy spectrum within the wave-dominated frequency range ($\int_{f_{wl}}^{f_{wu}} S_{v\beta}\mathrm{d}f$). For the example burst, β_1 is 164° (Fig. 5d).

(4) Estimating proportional constants: Proportional constants (C_{uv} and C_{wv}) between turbulent spectra in wave-wise ($S_{u\beta 1}$) and vertical ($S_{w\beta 1}$) directions relative to the cross-wave ($S_{v\beta 1}$) direction are determined at frequencies above f_{wu} to minimize wave influence:

$$C_{uv} = \frac{1}{f_{tu}\text{-}f_{wu}} \int_{f_{wu}}^{f_{tu}} \frac{S_{u\beta 1}}{S_{v\beta 1}} \mathrm{d}f \tag{4a}$$

$$C_{wv} = \frac{1}{f_{tu}\text{-}f_{wu}} \int_{f_{wu}}^{f_{tu}} \frac{S_{w\beta 1}}{S_{v\beta 1}} \mathrm{d}f \tag{4b}$$

where f_{tu} is the upper turbulence frequency limit (8 Hz in this study). To reduce biases induced by spectral spikes at high frequencies (Fig. 5e–g), a moving average window of $log_{10}(f)$ = 0.1 is applied for smoothing. Fig. 5h–i confirm the validity of the proportionality assumption. Averaging ratios at high frequencies (>0.5 Hz) determine the proportional constants. The estimated constants are representative, corresponding to the median constants estimated by the original spectra. Considering that proportional constants may vary under different flow conditions (e.g.,

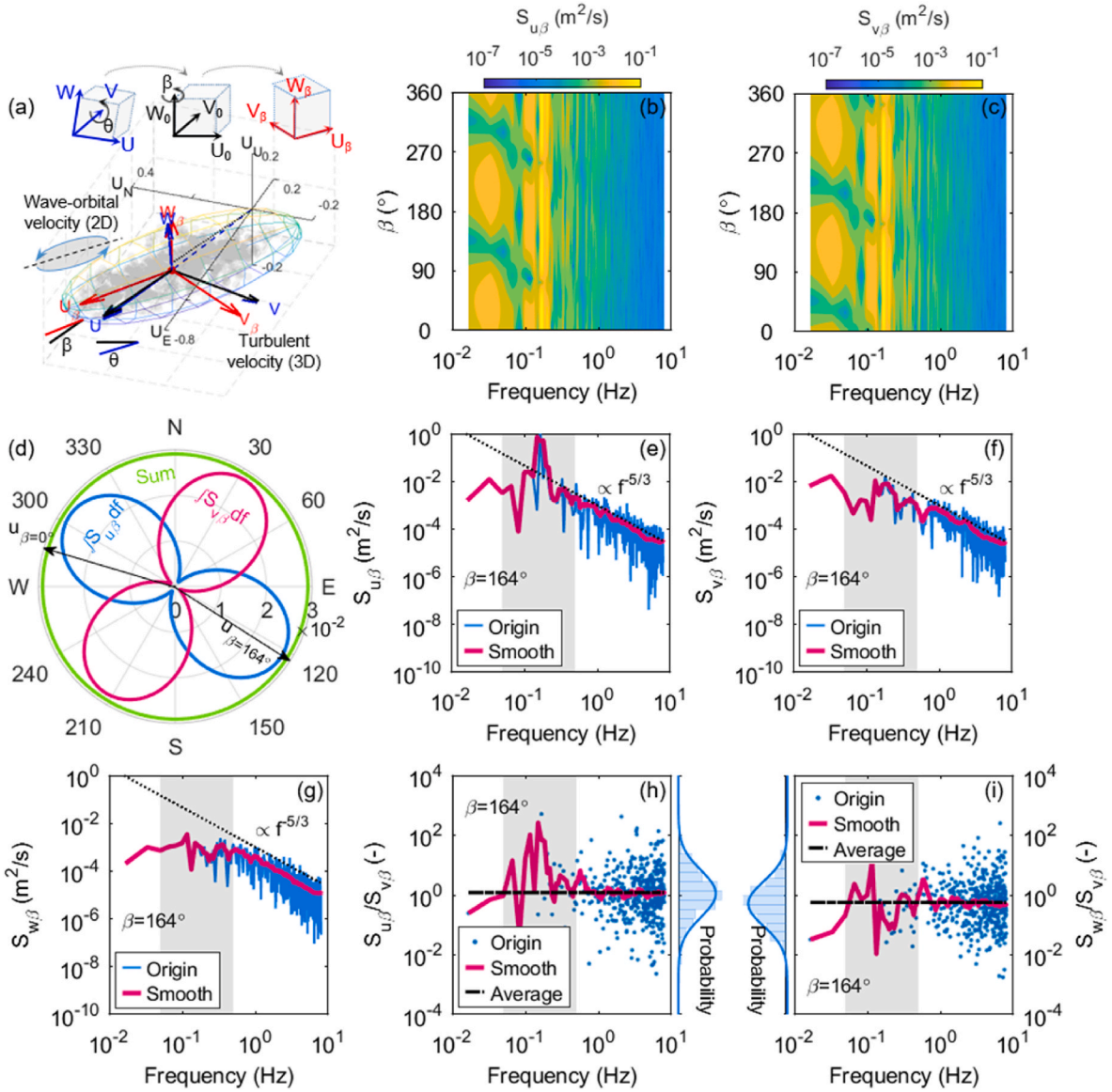

Fig. 5. (a) Illustration of the coordinate transformation and three-dimensional raw velocity fluctuations. The *U*, *V*, and *W* (blue) indicate stream-wise, cross-stream, and up-till directions. This coordinate system is rotated counter-clockwise around the *V* axis by an angle of θ to get the black one where U_0 and V_0 axes are on the horizontal plane, and W_0 is vertical. The red coordinate system (U_β, V_β, W_β) is obtained by rotating the black one (U_0, V_0, W_0) counter-clockwise around the W_0 axis by an angle β. (b–c) Power spectra density (PSD) of raw velocity fluctuations in U_β and V_β directions for each β. (d) Integrated PSD at wave frequencies (0.05–0.5 Hz). The arrow with $\beta = 0°$ indicates the stream-wise directions, and the one with $\beta = 164°$ indicates the wave direction where integrated PSD of velocities in U_β direction reaches the maximum and that in V_β direction reaches the minimum. (e–g) The original and smoothed spectra with $\beta = 164°$. (h–i) The ratios of wave-vise and vertical velocity spectra to the cross-wave. The dots show the ratios derived from the original spectrum, the solid line from the smoothed spectrum, and the dashed line averaged ratios outside the wave frequencies (grey area). The blue bars show the probability of original ratios with a Gaussian fitting curve. (For interpretation of the references to colour in this figure legend, the reader is referred to the Web version of this article.)

stratification and anisotropy), we recommend estimating them for each burst.

(5) Estimating turbulent spectra: Using the proportional constants and the cross-wave turbulent spectrum, wave-wise and vertical turbulent spectra are estimated within wave frequencies, while those outside the wave frequency range remain unchanged:

$$S'_{u\beta 1} = \begin{cases} S_{u\beta 1}, f \in (0, f_{wl}) \cup (f_{wu}, f_{tu}) \\ C_{uv} S_{v\beta 1}, f \in [f_{wl}, f_{wu}] \end{cases} \tag{5a}$$

$$S'_{v\beta 1} = S_{v\beta 1}, f \in (0, f_{tu}) \tag{5b}$$

$$S'_{w\beta 1} = \begin{cases} S_{w\beta 1}, f \in (0, f_{wl}) \cup (f_{wu}, f_{tu}) \\ C_{wv} S_{v\beta 1}, f \in [f_{wl}, f_{wu}] \end{cases} \tag{5c}$$

where $S'_{u\beta 1}$, $S'_{v\beta 1}$ and $S'_{w\beta 1}$ denote turbulent spectra in wave-wise, cross-wave, and vertical directions, respectively.

(6) Extracting wave-related spectra and energy: Wave-induced spectra are derived by subtracting turbulent spectra from the original ones:

$$S''_{u\beta 1} = S_{u\beta 1} - S'_{u\beta 1} \tag{6a}$$

$$S''_{v\beta 1} = S_{v\beta 1} - S'_{v\beta 1} = 0 \tag{6b}$$

$$S''_{w\beta 1} = S_{w\beta 1} - S'_{w\beta 1} \tag{6c}$$

where $S''_{u\beta 1}$, $S''_{u\beta 1}$ and $S''_{u\beta 1}$ are wave-related velocity spectra in wave-wise, cross-wave, and vertical directions, respectively. Wave kinetic energy (WKE, E_w) and turbulence kinetic energy (TKE, E_t) are calculated by integrating their respective spectra:

$$E_w = \int_0^{f_{tu}} S''_{u\beta 1} + S''_{w\beta 1} \mathrm{d}f \tag{7a}$$

$$E_t = \int_0^{f_{tu}} S'_{u\beta 1} + S'_{v\beta 1} + S'_{w\beta 1} \mathrm{d}f \tag{7b}$$

As a result, RoCoM effectively separates wave and turbulence components in both spectral and energy perspectives.

2.2.2. Methods for comparison

To evaluate the effectiveness of RoCoM, we conducted comparative analyses with three widely recognized wave-turbulence decomposition methods: MA, ESA, and SWT. Methods such as coherence, cospectra, linear wave theory, stopband filtering, EMD, and EEMD were excluded, as prior studies indicated these approaches provide less reliable turbulence estimates compared to SWT (Bian et al., 2018; Perez et al., 2020a, 2020b). Below, we detail the application of the MA, ESA, and SWT methods employed in our study.

The MA method employs a moving average filter to extract wave-induced velocity fluctuations, regarding the resulting smoothed signal as representative of wave orbital velocities (Williams et al., 2003). Typically, a 1-s averaging window has been recommended as it preserves turbulence energy more effectively compared to longer windows (Perez et al., 2020a; Williams et al., 2003). However, we selected a 2-s averaging window due to our specific wave frequency range (0.05–0.5 Hz, corresponding to wave periods of 2~20 s). This choice effectively preserved energy in the intermediate frequency band (0.5–1 Hz), yielding more accurate turbulence estimations than the 1-s window.

The ESA method decomposes variances in the frequency domain without directly separating instantaneous velocity fluctuations. Originally proposed by Soulsby and Humphrey (1990), ESA attributes variance above and below a baseline turbulent spectrum to wave and turbulence components, respectively, using the Kolmogorov −5/3 power law, as seen by Zhu et al. (2016). Recognizing that the Kolmogorov law requires isotropic turbulence conditions (Frisch, 1995), not typically met in stratified estuarine environments due to density stratification and wall effect, we adopted the modified approach of Bricker and Monismith (2007). Instead of assuming a predefined power law, we fitted a least-squares spectrum outside the wave band to accommodate observed deviations from isotropy due to stratification effects (Fig. 2a), thus enhancing the reliability of turbulence spectra estimates in the Changjiang Estuary. The resulting fitted curve replaced the original spectra within the wave band.

For the SWT method, we applied MATLAB-based algorithms developed by Thakur et al. (2013). Utilizing a Morlet wavelet with 64 voices, the SWT extracted wave-dominated fluctuations in the range of 0.05–0.5 Hz, subsequently subtracting these components from the original signal to isolate turbulent velocities.

To maintain consistent comparison standards, all methods, including RoCoM, were applied in the wave-oriented coordinate system ($U_{\beta 1}$, $V_{\beta 1}$, $W_{\beta 1}$). Unlike traditional stream-wise (U), cross-stream (V), and vertical (W) directions typically used by other methods, the wave-oriented coordinate system enabled a direct and fair assessment of RoCoM performance.

Due to the absence of a definitive turbulence reference, quantifying method uncertainty posed a challenge. To address this problem, we selected a reference burst (No. 2736, at 22:55, January 24), featuring similar hydrodynamic conditions but significantly lower wave heights compared to our test burst (No. 2 592). Both bursts, recorded during flood tides, had comparable mean flow directions (286.4° vs. 286.6°), velocities (0.38 m/s vs. 0.42 m/s), and well-mixed conditions (buoyancy frequencies $<0.01\ s^{-2}$). However, burst No. 2 736 had a wave height of 0.20 m, significantly lower than 1.16 m in burst No. 2 592. Given that turbulence energy scales with the squared flow velocity (Xu, 2009), we scaled the reference PSD by a factor of 1.2 to correct for the ~10 % velocity difference, ensuring robust comparative analysis.

Several factors ensure the reliability of this comparison. First, observations were conducted in the North Passage, a channelized region characterized by narrow wave directional spreading, aligning with RoCoM assumptions. Second, selecting well-mixed bursts, minimizing stratification-related biases, and allowing more precise differentiation between wave and turbulence contributions. We applied these methods to the entire observation series to further evaluate the applicability of RoCoM, MA, ESA, and SWT under stratified conditions (Section 3.2). Finally, applying velocity projections onto a standard wave-oriented coordinate system eliminated potential discrepancies arising from differing coordinate transformations, ensuring method comparisons were both direct and valid.

3. Results and discussion

3.1. Power spectra view of method performance

Fig. 6a–c presents the power spectra of raw velocity and turbulent fluctuations derived from the MA, ESA, SWT, and RoCoM methods. The MA operates as a low-pass filter, significantly attenuating spectral energy below 0.5 Hz, and therefore underestimates turbulent PSD by removing low-frequency turbulence along with wave signals (Fig. 6a–f). Compared to the reference burst (No. 2 736), the cumulative PSD estimated by the MA method is underestimated by 23 %, 40 %, and 7 % in the u, v, and w directions, respectively. Moreover, residual peaks remain at wave-dominated frequencies, indicating incomplete removal of wave orbital velocities, consistent with previous findings (Perez et al., 2020a).

In contrast, the ESA method tends to overestimate PSD at lower wave frequencies, despite accurately fitting high-frequency (>0.5 Hz) turbulence spectra (Fig. 6a–f). The extended spectral fitting line, which is based on data outside the wave peak, inadvertently inflates the PSD at lower frequencies that do not adhere strictly to Kolmogorov's inertial subrange. Consequently, PSDs are overestimated by approximately 5 %, 46 %, and 97 % in the u, v, and w directions, respectively.

The SWT and RoCoM methods show minimal influence on spectral energy outside wave-dominated frequencies (highlighted by the shaded area in Fig. 6a–f). The SWT employs wavelet analysis and synchrosqueezing to effectively concentrate energy and mitigate mode-mixing issues (Daubechies et al., 2011). However, due to the inherent challenges of distinguishing wave-induced from turbulence-induced fluctuations at overlapping frequencies, the SWT method inadvertently removes a portion of turbulence energy, creating a distinct energy trough in the turbulent spectrum (Fig. 6a–f). This effect, also observed with other EMD-based methods (Bian et al., 2018; Perez et al., 2020a; Qiao et al., 2016), leads to significant PSD underestimations of up to 50 %, 35 %, and 22 % in the u, v, and w directions, respectively.

The RoCoM method, however, successfully retains turbulence energy at wave-dominated frequencies, providing PSD estimates closely aligning with the reference spectrum and the expected power law behavior (Fig. 6a–f). The wave energy peak in the u direction is substantially reduced, indicating effective wave energy removal (Fig. 6a and d). A minor residual peak in the v direction persists due to potential wave-turbulence interactions (Fig. 6b). Consequently, PSDs are slightly overestimated by approximately 2 %, 25 %, and 60 % in the u, v, and w directions, respectively. While the w-direction exhibits notable uncertainty, its impact on overall TKE estimation remains minor, as w fluctuations contribute only 13 % to the total turbulence.

Further validation using in-lab experimental data supports the

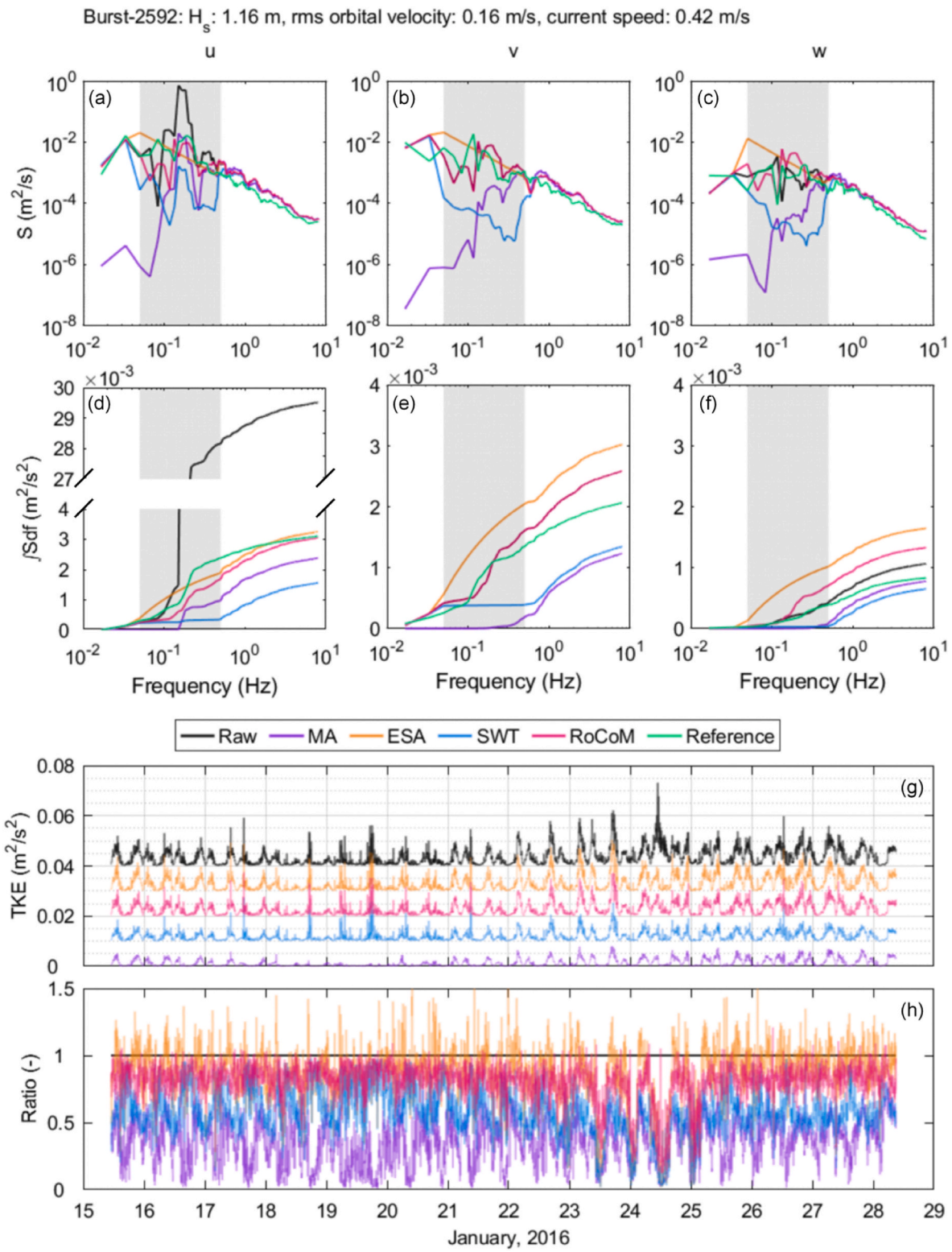

Fig. 6. The evaluation of wave-turbulence decomposition methods with in-situ measurements in the Changjiang Estuary. (a–c) Power spectra of raw velocity fluctuations and the turbulent fluctuations estimated by the MA, ESA, SWT, and RoCoM methods in (a) wave-wise (u), (b) cross-wave (v), and (c) vertical (w) directions for burst No. 2 592. For clarity, the spectrum is smoothed with a window of $log_{10}(f) = 0.1$, where f is frequency. (d–f) Cumulative power spectra of turbulent fluctuations by the various methods for (d) u, (e) v, and (f) w for burst No. 2 592. The grey area shows the wave-dominated frequency range. The green lines indicate the results of the reference burst (No. 2 736) with similar velocity and stratification conditions as burst No. 2 592 but a much lower wave height. Time series of (g) turbulent kinetic energy (TKE) estimated by raw velocity fluctuations and the turbulent fluctuations given by various methods and (h) their ratios to the original one. Note that the TKE basis for each method is shifted by 0.01 m^2/s^2 for clarity of the graph. (For interpretation of the references to colour in this figure legend, the reader is referred to the Web version of this article.)

superior performance of the RoCoM method among the evaluated techniques (Fig. 7). Comparing estimated turbulence spectra against controlled reference spectra, RoCoM yielded relative errors of 16 %, 12 %, and 72 % in the *u*, *v*, and *w* directions, respectively. For comparison, the MA method resulted in relative errors of 27 %, 20 %, and 18 %, while the ESA method had relative errors of 18 %, 29 %, and 92 %. The SWT method significantly underestimated turbulence energy, with relative errors of 52 %, 35 %, and 1 % in the *u*, *v*, and *w* directions, respectively. These experimental results confirm that RoCoM consistently provides the most accurate turbulence spectral estimates, particularly under laboratory-controlled conditions.

3.2. TKE estimation by various methods

TKE, defined as $\frac{1}{2}\left(\overline{u'^2} + \overline{v'^2} + \overline{w'^2}\right)$, where the apostrophe denotes turbulent velocity fluctuations, was calculated by integrating turbulent PSDs across all three velocity components. For the sample burst (No. 2 592), the MA, ESA, SWT, and RoCoM methods yielded TKE estimates with biases of −27 %, 32 %, −40 %, and 16 %, respectively (Fig. 8a). While the RoCoM method slightly overestimated the TKE, it provides the most accurate overall estimate. In contrast, the MA and SWT methods underestimated TKE due to excessive removal of turbulence energy within the wave-dominated and lower frequency ranges. Conversely, the ESA method substantially overestimated TKE, as it extends the turbulent spectral fitting into frequencies beyond Kolmogorov's inertial subrange, causing notable deviations from the theoretical power-law spectrum.

We applied the MA, ESA, SWT, and RoCoM methods to comprehensively evaluate method stability and applicability across all 3721 data bursts. During the storm event between January 23 and 25, raw energy, calculated as the sum of the PSDs from original velocity measurements, exhibited significant fluctuations (Figs. 2 and 6g). Fig. 6g demonstrates that all methods effectively removed wave energy during storm conditions and showed consistent TKE variations throughout the observation period, albeit with occasional deviations. Specifically, the ESA method generally yielded higher TKE estimates, while the MA and SWT methods consistently underestimated TKE relative to the RoCoM method (Fig. 6h). Under calm conditions, the ESA method overestimated TKE, whereas the MA and SWT underestimated it, with RoCoM providing estimates closest to the raw data. These results collectively demonstrate the robustness and applicability of RoCoM across diverse wave conditions.

Further validation with controlled in-lab experiments, as illustrated in Fig. 8, confirmed the superior accuracy of RoCoM in estimating TKE, particularly within the wave-dominated frequency band. The relative errors in TKE estimation by the MA, ESA, SWT, and RoCoM methods from both in situ and laboratory datasets are summarized in Fig. 8. For the laboratory experiments (Fig. 8b), the relative errors in total TKE estimates were −15 % (MA), 23 % (ESA), −35 % (SWT), and 14 % (RoCoM), and the errors in wave-band TKE were −66 % (MA), 25 % (ESA), −97 % (SWT), and 7 % (RoCoM). These detailed comparative

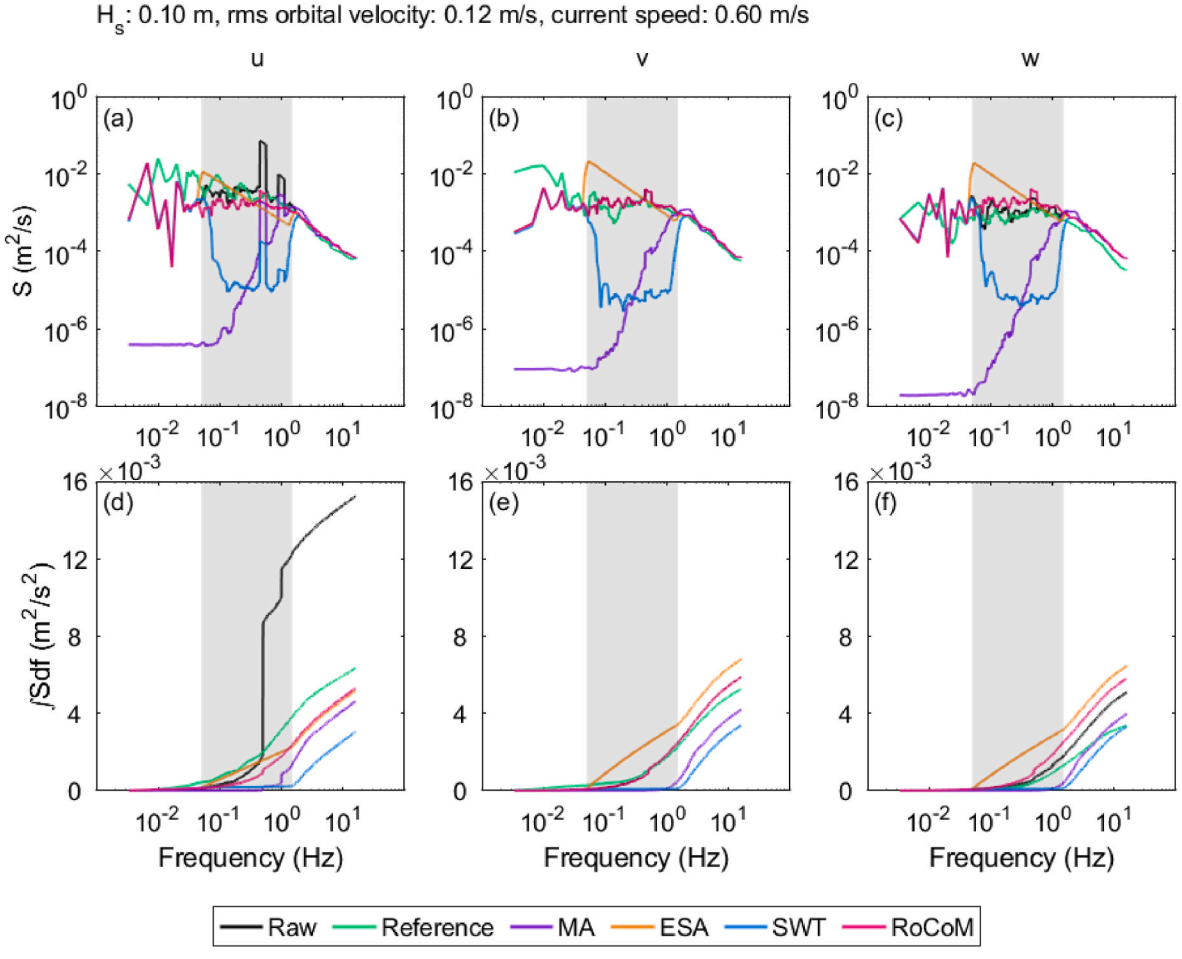

Fig. 7. The evaluation of wave-turbulence decomposition methods with data from in-lab experiments. (a–c) Power spectra of raw velocity fluctuations and the turbulent fluctuations estimated by the MA, ESA, SWT, and RoCoM methods in (a) wave-wise (*u*), (b) cross-wave (*v*), and (c) vertical (*w*) directions. For clarity, the spectrum is smoothed with a window of $log_{10}(f) = 0.1$, where *f* is frequency. (d–f) Cumulative power spectra of turbulent fluctuations by the various methods for (d) *u*, (e) *v*, and (f) *w*. The grey area shows the wave-dominated frequency range. The green lines indicate the results of the reference burst with the same velocity but no waves. (For interpretation of the references to colour in this figure legend, the reader is referred to the Web version of this article.)

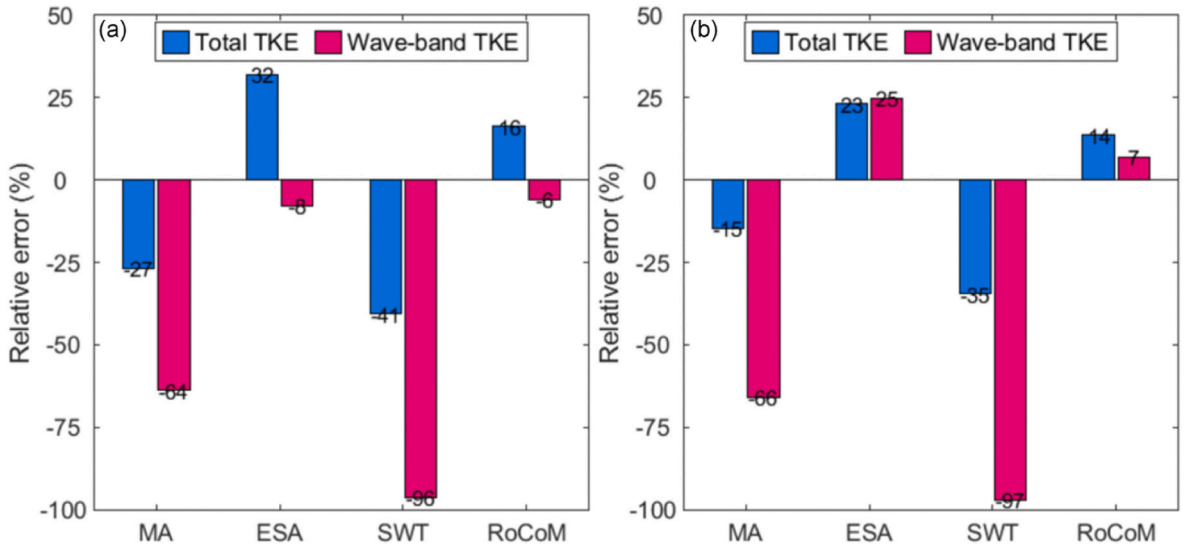

Fig. 8. Relative error of turbulent kinetic energy (TKE) estimated by the MA, ESA, SWT, and RoCoM methods for (a) in situ measurements and (b) lab experiments. Blue bars represent the bias in total TKE, and red bars show those in wave-band TKE (i.e., TKE within the wave-dominated frequency band). (For interpretation of the references to colour in this figure legend, the reader is referred to the Web version of this article.)

results explicitly demonstrate the consistent ability of RoCoM to deliver the most accurate TKE estimations under both field and laboratory conditions.

3.3. Limitations and future outlook

To streamline computational procedures, this study initially identified the principal wave direction by selecting the maximum integrated PSD at wave frequencies. However, this simplified approach is appropriate when wave orbital velocities notably exceed mean flow velocities. Under conditions where mean flow velocities are comparable to or exceed wave velocities, this method could misidentify mean flow as the wave direction, potentially affecting accuracy. Nevertheless, under these conditions, wave energy is usually minimal relative to turbulence energy, thus limiting RoCoM estimation bias. For enhanced precision, we recommend employing the "PUV method" (Herbers et al., 1999) to robustly determine the principal wave direction, particularly in scenarios with relatively lower wave energies.

As shown in Fig. 6b, the RoCoM method retains a minor residual spectral peak at wave frequencies. This residual peak likely arises from wave-turbulence interactions and/or wide directional wave spreading. Although cross-wave velocity spectra ($S_{v\beta 1}$) remain largely unaffected by wave orbital motions, they may still experience some influence from wave-induced turbulence. Observational data indicated minimal wave directional spreading during the survey, as swell wave propagation directions aligned closely with wind directions, primarily perpendicular to the coastline. Hence, the observed residual spectral peaks mainly resulted from wave-turbulence interactions. Wave-turbulence interactions enhance turbulence intensity, facilitating energy transfer from wave motions to turbulence through turbulent viscosity, and consequently generating identifiable peaks within turbulence spectra (Huang and Qiao, 2010; Smeltzer et al., 2023). Even in non-breaking wave conditions, wave-induced turbulence has been documented (Babanin and Haus, 2009).

However, if waves propagate significantly in multiple directions, the RoCoM method will primarily remove the energy of the most dominant wave component, potentially leaving residual wave energy in the cross-wave component ($S_{v\beta 1}$). This residual energy complicates the decomposition process. Therefore, the RoCoM method is most appropriate in environments characterized by narrow directional wave spreading, conditions frequently encountered in coastal and nearshore environments globally (Herbers et al., 1999; Le Merle et al., 2021; Sundar et al., 1998).

Further limitations of RoCoM include its inability to reconstruct wave and turbulence velocity time series, as it operates exclusively within the power spectral domain, similarly to the ESA method. This contrasts with the SWT method, which effectively reconstructs wave and turbulence velocity time series, enabling direct assessments of turbulent Reynolds stresses and wave orbital velocities.

Given these constraints, the SWT method is preferable in environments with substantial wave directional spreading due to its robustness under strong wave conditions and its capability for direct velocity reconstruction. Specifically, SWT reliably differentiates wave-induced motions from turbulence under strong wave conditions and provides distinct advantages over the ESA and MA methods under weak wave conditions. Nonetheless, future work should enhance the applicability of RoCoM by addressing its limitations in velocity reconstruction and performance under conditions of broader wave directional spreading.

4. Summary

This study introduces a novel wave-turbulence decomposition method, RoCoM, which utilizes energy spectrum analysis. The RoCoM approach is grounded in two key physical assumptions. First, it assumes that the turbulence energy spectrum in the cross-wave direction ($S_{v\beta 1}$) is unaffected by wave orbital velocities. This assumption is valid predominantly under narrow directional wave spreading conditions, commonly observed in coastal regions with minimal reflection effects. The cross-wave direction is the orientation in which the integrated PSD at wave frequencies reaches its minimum. Second, RoCoM presumes that turbulence spectra in the wave-wise (u) and vertical (w) directions are proportionally related to $S_{v\beta 1}$ within the wave frequency range. This assumption implies that turbulence maintains a consistent three-dimensional fractal structure across various frequency scales. The proportional constants required for this calculation are determined by averaging the spectral ratios at higher frequencies outside the wave-dominated frequency range. These constants are subsequently used to estimate turbulent u and w spectra at wave frequencies by multiplying the constants by $S_{v\beta 1}$. Empirical observations from the Changjiang Estuary substantiate the validity of these two assumptions.

To assess the performance of RoCoM, we conducted comparative evaluations with the MA, ESA, and SWT methods. Our analyses included

assessments of power spectra, TKE estimates, and associated uncertainties. Results demonstrated that all tested methods effectively remove wave energy, yielding TKE estimates exhibiting similar magnitudes and temporal variations. Among these methods, RoCoM provided the most accurate TKE estimates by effectively addressing wave-turbulence interactions, demonstrating a minor overestimation of approximately 16 % for in-situ observations and 14 % for in-lab experiments. The biases are as low as 6–7 % for wave-band TKE. In contrast, ESA significantly overestimated TKE (32 %) due to deviations of low-frequency fluctuations from the assumed power-law spectrum. The MA and SWT methods tended to underestimate TKE by approximately 27 % and 40 %, respectively, because they inadvertently removed some turbulence and wave energy at wave-dominated and lower frequencies. Notably, SWT remains advantageous under conditions of significant wave-directional spreading, as it allows reliable reconstruction of wave and turbulence velocity time series, facilitating direct estimation of turbulent Reynolds stress and wave orbital velocities. Therefore, SWT is recommended for application in environments featuring significant, broader wave-directional spreading.

In conclusion, RoCoM demonstrates superior performance as an effective wave-turbulence decomposition method under both weak and strong wave conditions. Nonetheless, the current implementation of RoCoM is optimal for scenarios with narrow directional-spreading waves. Further research efforts should thus focus on extending the RoCoM applicability to accommodate scenarios involving multidirectional wave propagation.

CRediT authorship contribution statement

Jianliang Lin: Writing – review & editing, Writing – original draft, Visualization, Validation, Project administration, Methodology, Investigation, Funding acquisition, Formal analysis, Data curation, Conceptualization. **Chunyan Zhu:** Writing – review & editing, Investigation. **Jianwei Sun:** Writing – review & editing, Methodology. **Weiming Xie:** Writing – review & editing, Methodology. **Bram van Prooijen:** Writing – review & editing, Formal analysis. **Leicheng Guo:** Writing – review & editing, Methodology. **Qing He:** Writing – review & editing, Project administration, Funding acquisition. **Qingshu Yang:** Writing – review & editing. **Zheng Bing Wang:** Writing – review & editing, Project administration, Funding acquisition.

Declaration of competing interest

The authors declare that they have no known competing financial interests or personal relationships that could have appeared to influence the work reported in this paper.

Acknowledgments

This study is supported by the National Natural Science Foundation of China (No. 42406159). This work is partly supported by the project "Coping with Deltas in Transition", financed by the Chinese Ministry of Science and Technology (MOST), Project No. 2016YFE0133700, and the Royal Netherlands Academy of Arts and Sciences (KNAW), Project No. PSA-SA-E-02. The data used for elaborating and testing the RoCoM in the study are available at figshare via https://figshare.com/s/2cd6d86b38b720141083.

Data availability

Data will be made available on request.

References

Amoudry, L.O., Souza, A.J., 2011. Deterministic coastal morphological and sediment transport modeling: a review and discussion. Rev. Geophys. 49, 1–21. https://doi.org/10.1029/2010RG000341.

Babanin, A.V., Haus, B.K., 2009. On the existence of water turbulence induced by nonbreaking surface waves. J. Phys. Oceanogr. 39, 2675–2679. https://doi.org/10.1175/2009JPO4202.1.

Benilov, A.Y., Kouznetsov, O.A., Panin, G.N., 1974. On the analysis of wind wave-induced disturbances in the atmospheric turbulent surface layer. Boundary-Layer Meteorol. 6, 269–285. https://doi.org/10.1007/BF00232489.

Bian, C., Liu, Z., Huang, Y., Zhao, L., Jiang, W., 2018. On estimating turbulent Reynolds stress in wavy aquatic environment. J. Geophys. Res. Ocean. 123, 3060–3071. https://doi.org/10.1002/2017JC013230.

Brand, A., Lacy, J.R., Hsu, K., Hoover, D., Gladding, S., Stacey, M.T., 2010. Wind-enhanced resuspension in the shallow waters of South San Francisco Bay: mechanisms and potential implications for cohesive sediment transport. J. Geophys. Res. Ocean. 115, 1–15. https://doi.org/10.1029/2010JC006172.

Bricker, J.D., Monismith, S.G., 2007. Spectral wave-turbulence decomposition. J. Atmos. Ocean. Technol. 24, 1479–1487. https://doi.org/10.1175/JTECH2066.1.

Copping, A., Battey, H., Brown-Saracino, J., Massaua, M., Smith, C., 2014. An international assessment of the environmental effects of marine energy development. Ocean Coast Manag. 99, 3–13. https://doi.org/10.1016/j.ocecoaman.2014.04.002.

Daubechies, I., Lu, J., Wu, H.T., 2011. Synchrosqueezed wavelet transforms: an empirical mode decomposition-like tool. Appl. Comput. Harmon. Anal. 30, 243–261. https://doi.org/10.1016/j.acha.2010.08.002.

Frisch, U., 1995. Turbulence: the Legacy of A. N. Kolmogorov. Cambridge Univ. Press, New York.

Gerbi, G.P., Trowbridge, J.H., Edson, J.B., Plueddemann, A.J., Terray, E.A., Fredericks, J. J., 2008. Measurements of momentum and heat transfer across the air-sea interface. J. Phys. Oceanogr. 38, 1054–1072. https://doi.org/10.1175/2007JPO3739.1.

Goring, D.G., Nikora, V.I., 2002. Despiking acoustic Doppler velocimeter data. J. Hydraul. Eng. 128, 117–126. https://doi.org/10.1061/(ASCE)0733-9429(2002)128:1(117.

Guo, C., He, Q., Guo, L., Winterwerp, J.C., 2017. A study of in-situ sediment flocculation in the turbidity maxima of the Yangtze Estuary. Estuar. Coast Shelf Sci. 191, 1–9. https://doi.org/10.1016/j.ecss.2017.04.001.

Harrold, M., Ouro, P., 2019. Rotor loading characteristics of a full-scale tidal turbine. Energies 12, 1035. https://doi.org/10.3390/en12061035.

Herbers, T.H.C., Elgar, S., Guza, 1999. Directional spreading of waves in the nearshore zone. J. Geophys. Res. 104, 7683–7693. https://doi.org/10.1029/1998JC900092.

Huang, C.J., Qiao, F., 2010. Wave-turbulence interaction and its induced mixing in the upper ocean. J. Geophys. Res. Ocean. 115, C04026. https://doi.org/10.1029/2009JC005853.

Huang, N.E., Hu, K., Yang, A.C.C., Chang, H.C., Jia, D., Liang, W.K., Yeh, J.R., Kao, C.L., Juan, C.H., Peng, C.K., Meijer, J.H., Wang, Y.H., Long, S.R., Wu, Z., 2016. On holo-hilbert spectral analysis: a full informational spectral representation for nonlinear and non-stationary data. Philos. Trans. R. Soc. A Math. Phys. Eng. Sci. 374, 20150206. https://doi.org/10.1098/rsta.2015.0206.

Huang, N.E., Shen, Z., Long, S.R., Wu, M.C., Snin, H.H., Zheng, Q., Yen, N.C., Tung, C.C., Liu, H.H., 1998. The empirical mode decomposition and the Hubert spectrum for nonlinear and non-stationary time series analysis. Proc. R. Soc. A Math. Phys. Eng. Sci. 454, 903–995. https://doi.org/10.1098/rspa.1998.0193.

Huang, N.E., Wu, M.L.C., Long, S.R., Shen, S.S.P., Qu, W., Gloersen, P., Fan, K.L., 2003. A confidence limit for the empirical mode decomposition and Hilbert spectral analysis. Proc. R. Soc. A Math. Phys. Eng. Sci. 459, 2317–2345. https://doi.org/10.1098/rspa.2003.1123.

Kaimal, J.C., Wyngaard, J.C., Izumi, Y., Coté, O.R., 1972. Spectral characteristics of surface-layer turbulence. Q. J. R. Meteorol. Soc. 98, 563–589. https://doi.org/10.1002/qj.49709841707.

Kirincich, A.R., 2013. Long-term observations of turbulent Reynolds stresses over the inner continental shelf. J. Phys. Oceanogr. 43, 2752–2771. https://doi.org/10.1175/JPO-D-12-0153.1.

Kirincich, A.R., Lentz, S.J., Gerbi, G.P., 2010. Calculating Reynolds stresses from ADCP measurements in the presence of surface gravity waves using the cospectra-fit method. J. Atmos. Ocean. Technol. 27, 889–907. https://doi.org/10.1175/2009JTECHO682.1.

Kirincich, A.R., Rosman, J.H., 2011. A comparison of methods for estimating Reynolds stress from ADCP measurements in wavy environments. J. Atmos. Ocean. Technol. 28, 1539–1553. https://doi.org/10.1175/JTECH-D-11-00001.1.

Le Merle, E., Hauser, D., Peureux, C., Aouf, L., Schippers, P., Dufour, C., Dalphinet, A., 2021. Directional and frequency spread of surface ocean waves from SWIM measurements. J. Geophys. Res. Ocean. 126, e2021JC017220. https://doi.org/10.1029/2021JC017220.

Li, R., Voulgaris, G., Wang, Y.P., 2022. Turbulence structure and burst events observed in a tidally induced bottom boundary layer. J. Geophys. Res. Ocean. 127. https://doi.org/10.1029/2021JC018036.

Lin, J., He, Q., Guo, L., van Prooijen, B.C., Wang, Z.B., 2020. An integrated optic and acoustic (IOA) approach for measuring suspended sediment concentration in highly turbid environments. Mar. Geol. 421, 106062. https://doi.org/10.1016/j.margeo.2019.106062.

Lumley, J.L., Terray, E.A., 1983. Kinematics of turbulence convected by a random wave field. J. Phys. Oceanogr. 13, 2000–2007. https://doi.org/10.1175/1520-0485(1983)013<2000:KOTCBA>2.0.CO;2.

MacVean, L.J., Lacy, J.R., 2014. Interactions between waves, sediment, and turbulence on a shallow estuarine mudflat. J. Geophys. Res. Ocean. 119, 1534–1553. https://doi.org/10.1002/2013JC009477.

McCaffrey, K., Fox-Kemper, B., Hamlington, P.E., Thomson, J., 2015. Characterization of turbulence anisotropy, coherence, and intermittency at a prospective tidal energy site: observational data analysis. Renew. Energy 76, 441–453. https://doi.org/10.1016/j.renene.2014.11.063.

Millero, F., Poisson, A., 1981. International one atmosphere equation of state of seawater. Deep Sea Res. 28A, 625–629.

Perez, L., Cossu, R., Couzi, C., Penesis, I., 2020a. Wave-turbulence decomposition methods applied to tidal energy site assessment. Energies 13, 1245. https://doi.org/10.3390/en13051245.

Perez, L., Cossu, R., Grinham, A., Penesis, I., 2020b. Evaluation of wave-turbulence decomposition methods applied to experimental wave and grid-generated turbulence data. Ocean Eng. 218, 108186. https://doi.org/10.1016/j.oceaneng.2020.108186.

Qiao, F., Yuan, Y., Deng, J., Dai, D., Song, Z., 2016. Wave-turbulence interaction-induced vertical mixing and its efects in ocean and climate models. Philos. Trans. R. Soc. A Math. Phys. Eng. Sci. 374, 20150201. https://doi.org/10.1098/rsta.2015.0201.

Rosman, J.H., Gerbi, G.P., 2017. Interpreting fixed-location observations of turbulence advected by waves: insights from spectral models. J. Phys. Oceanogr. 47, 909–931. https://doi.org/10.1175/JPO-D-15-0249.1.

Rosman, J.H., Hench, J.L., Koseff, J.R., Monismith, S.G., 2008. Extracting Reynolds stresses from acoustic Doppler current profiler measurements in wave-dominated environments. J. Atmos. Ocean. Technol. 25 (1), 286–306. https://doi.org/10.1175/2007JTECHO525.

Shaw, W.J., Trowbridge, J.H., 2001. The direct estimation of near-bottom turbulent fluxes in the presence of energetic wave motions. J. Atmos. Ocean. Technol. 18, 1540–1557. https://doi.org/10.1175/1520-0426(2001)018<1540:TDEONB>2.0.CO;2.

Smeltzer, B.K., Rømcke, O., Hearst, R.J., Ellingsen, S.Å., 2023. Experimental study of the mutual interactions between waves and tailored turbulence. J. Fluid Mech. 962, R1. https://doi.org/10.1017/jfm.2023.280.

Song, S., Santos, I.R., Yu, H., Wang, F., Burnett, W.C., Bianchi, T.S., Dong, J., Lian, E., Zhao, B., Mayer, L., Yao, Q., Yu, Z., Xu, B., 2022. A global assessment of the mixed layer in coastal sediments and implications for carbon storage. Nat. Commun. 13, 4903. https://doi.org/10.1038/s41467-022-32650-0.

Soulsby, R.L., Humphrey, J.D., 1990. Field observations of wave-current interaction at the sea bed. In: Tørum, A., Gudmestad, O.T. (Eds.), Water Wave Kinematics. Kluwer Academic Publishers, Dordrecht, The Netherlands, pp. 413–428. https://doi.org/10.1007/978-94-009-0531-3_25.

Sundar, V., Sannasiraj, S.A., Kaldenhoff, H., 1998. Directional spreading of waves in the nearshore zone. Ocean Eng. 26, 161–188. https://doi.org/10.1016/S0029-8018(97)00040-1.

Thakur, G., Brevdo, E., Fučkar, N.S., Wu, H.T., 2013. The Synchrosqueezing algorithm for time-varying spectral analysis: robustness properties and new paleoclimate applications. Signal Process. 93, 1079–1094. https://doi.org/10.1016/j.sigpro.2012.11.029.

Trowbridge, J.H., 1998. On a technique for measurement of turbulent shear stress in the presence of surface waves. J. Atmos. Ocean. Technol. 15, 290–298. https://doi.org/10.1175/1520-0426(1998)015<0290:oatfmo>2.0.co;2.

Trowbridge, J.H., Lentz, S.J., 2018. The bottom boundary layer. Ann. Rev. Mar. Sci 10, 397–420. https://doi.org/10.1146/annurev-marine-121916-063351.

Tucker, M.J., Pitt, E.G., 2001. Waves in Ocean Engineering, Elsevier Ocean Engineering Book Sereis. Elsevier, Amsterdam. https://doi.org/10.1016/0141-0296(92)90048-u.

Veers, P., Dykes, K., Lantz, E., Barth, S., Bottasso, C.L., Carlson, O., Clifton, A., Green, J., Green, P., Holttinen, H., Laird, D., Lehtomäki, V., Lundquist, J.K., Manwell, J., Marquis, M., Meneveau, C., Moriarty, P., Munduate, X., Muskulus, M., Naughton, J., Pao, L., Paquette, J., Peinke, J., Robertson, A., Rodrigo, J.S., Sempreviva, A.M., Smith, J.C., Tuohy, A., Wiser, R., 2019. Grand challenges in the science of wind energy. Science 366, 1–18. https://doi.org/10.1126/science.aau2027.

Wang, Y.-H., Yeh, C.-H., Young, H.-W.V., Hu, K., Lo, M.-T., 2014. On the computational complexity of the empirical mode decomposition algorithm. Phys. A Stat. Mech. its Appl. 400, 159–167. https://doi.org/10.1016/j.physa.2014.01.020.

Wiberg, P.L., Sherwood, C.R., 2008. Calculating wave-generated bottom orbital velocities from surface-wave parameters. Comput. Geosci. 34, 1243–1262. https://doi.org/10.1016/j.cageo.2008.02.010.

Williams, J.J., Bell, P.S., Thorne, P.D., 2003. Field measurements of flow fields and sediment transport above mobile bed forms. J. Geophys. Res. Ocean. 108, 3109. https://doi.org/10.1029/2002jc001336.

Wu, Z., Huang, N.E., 2009. Ensemble empirical mode decomposition: a noise-assited data analysis method. Adv. Adapt. Data Anal. 1, 1–41. https://doi.org/10.1142/S1793536909000047.

Wu, Z., Huang, N.E., 2004. A study of the characteristics of white noise using the empirical mode decomposition method. Proc. R. Soc. A Math. Phys. Eng. Sci. 460, 1597–1611. https://doi.org/10.1098/rspa.2003.1221.

Xu, J., 2009. Study on Near Bottom Dynamics and Sediment Processes in Turbidity Maximum. East China Normal University, China. MSc thesis. (in Chinese with English abstract).

Zhu, Q., van Prooijen, B.C., Wang, Z.B., Ma, Y.X., Yang, S.L., 2016. Bed shear stress estimation on an open intertidal flat using in situ measurements. Estuar. Coast Shelf Sci. 182, 190–201. https://doi.org/10.1016/j.ecss.2016.08.028.